ACS OMEGA

http://pubs.acs.org/journal/acsodf

Article

Treatment of Groundwater-Rich Organic Compounds Using Activated Carbon with Additional Germanium Dioxide (GeO_2): Kinetics and Adsorption Studies of Methylene Blue and Congo Red

Yulia Fajriani, Heryanto Heryanto, and Dahlang Tahir*

Cite This: *ACS Omega* 2023, 8, 27663−27673

Read Online

ACCESS | Metrics & More | Article Recommendations

ABSTRACT: Activated carbon/GeO_2 composites were synthesized using the sol−gel method and then used as catalysts for the photodegradation of organic pollutants methylene blue (MB) and congo red (CR). The composites were characterized using an X-ray diffractometer and Fourier transform infrared spectroscopy to analyze the structure and chemical bonds of the composite materials, respectively. The ultraviolet−visible (UV−vis) absorption wavelength ranges of the composites toward the pollutants were 550−700 nm for MB and 450−550 for CR. The band gap energies of the composites were calculated, with the values found to be <4.5 eV. It was shown that the adsorption ability of the composites increased with the irradiation time of the pollutants. Furthermore, the adsorption kinetics data were found to be a good fit to a pseudo-first-order kinetics model.

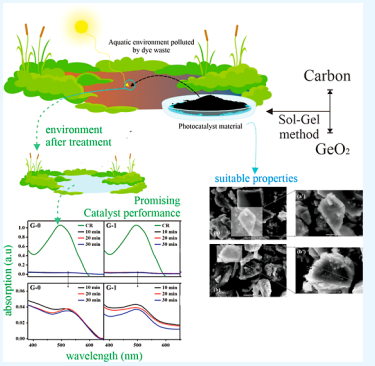

1. INTRODUCTION

The availability of clean water is a global issue that affects the health and quality of life of humans, plants, and animals.[1−5] This crisis is driven by several factors, one of which is the increase in the human population, leading to increased demand in the industrial sector.[6−11] The textile dye industry produces wastewater,[9,12,13] containing cationic and azo dyes, which are harmful to the human body if consumed.[9,13,14] Wastewater can be treated using advanced oxidation processes (AOPs), which involve the formation of hydroxyl radicals ($OH^•$) in adequate amounts for the cleansing of water.[9,10,15] AOPs can be divided into several group, such as photo-Fenton reactions, ozone oxidation, ultrasonic cavitation, and photocatalytic oxidation.[9,15,16]

Photocatalysis is one of the best methods for degrading pollutants present in water, as it does not require much energy in their process.[17] Photocatalytic reactions proceed if the catalysts contain electron−hole (e^-−h^+) pairs,[18,19] making it possible for oxidation and reduction processes to occur. Semiconductors such as TiO_2[20−23] and ZnO[24−27] are widely used as photocatalysts. However, in spite of the low toxicity and chemical stability properties[10,26] of these semiconductors, they exhibit swift recombination of the photogenerated e^-−h^+ pair, which lowers their photocatalytic performance.[26,28,29] Besides the swift recombination, another key factors that needs to be taken into consideration is the photocatalyst absorption range.[17] If the band gap of the photocatalyst is too narrow, it will cause overlapping, whereas if the bandgap is too wide, it will require a large amount of energy to excite electrons from the valence band (VB) to the conduction band (CB).

Activated carbon (AC) has been widely used as a support material for photocatalyst processes,[21,22,25,27] due to the fact that it possesses an ability to adsorb pollutant organic molecules on its surface. This ability is driven by the structure of AC, i.e., its high porosity and many active sites due to its high specific surface area.[23,24,29] In this study, AC was synthesized with the addition of GeO_2 via the sol−gel method. The addition of GeO_2 into AC was expected to extend the absorption range of AC to enable it to deal with various types of pollutants with diverse absorption wavelengths, due to the absorption range of GeO_2 in the near-ultraviolet (UV) region.[30,31] The performance of different AC/GeO_2 composites was then tested against the organic dye pollutants methylene blue (MB) and congo red (CR), which were subjected to photocatalysis utilizing optical lamps as a substitute for sunlight.

Received: May 20, 2023
Accepted: June 9, 2023
Published: July 18, 2023

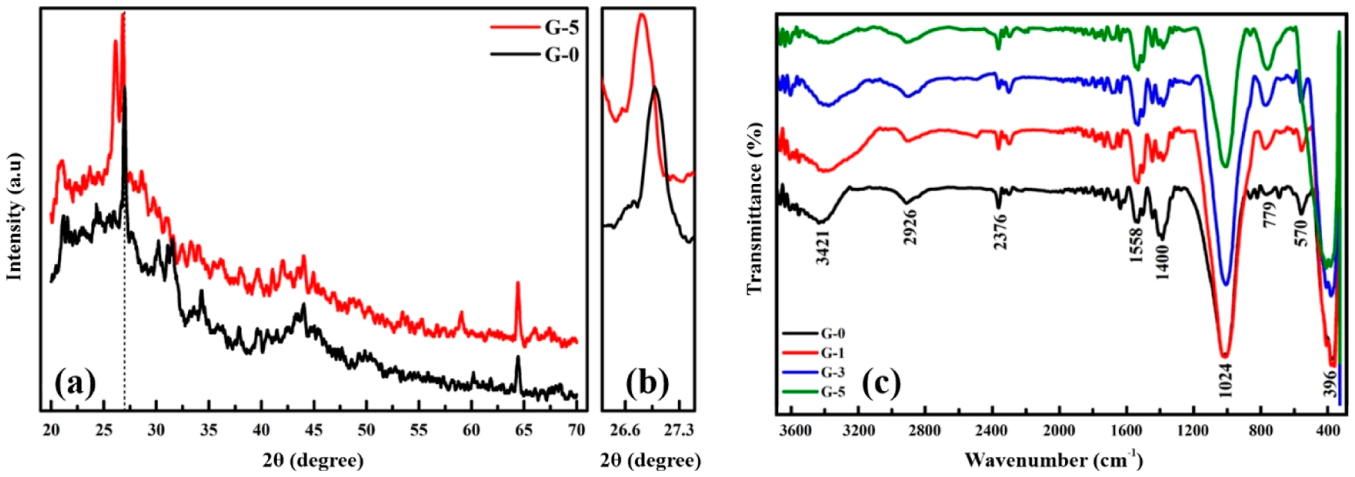

Figure 1. XRD spectra of G-0 and G-5 (a) at 2θ = 20−70° and (b) at 2θ = 26.3−27.5°; (c) FTIR spectrum of G-0, G-1, G-3, and G-5 at a wavelength of 3698−300 cm^{-1}.

2. EXPERIMENTAL SECTION

2.1. Materials. GeO_2 powder (99.999% purity) was purchased from Changsha Easchem Co., China. AC (surface area > 240 m/g, purity >95%, and average diameter < 10 μm) was supplied by PT. Cahaya Indo Abadi Indonesia. MB, CR, and ethanol (98%) were provided by CV. Intraco.

2.2. Synthesis AC/GeO_2 Composites. The AC used in this study was prepared according to a previously reported method.[32] The synthesis was carried out according to a literature preparation,[20] with some adjustments. AC (9.9 g) and GeO_2 (0.1 g) were placed in a 200 mL beaker, followed by the addition of ethanol (100 mL), while stirring for 15 min using a magnetic stirrer set at 200 rpm. After this process, the mixture was heated in an oven at 120 °C for 6 h and the composite obtained was referred to as G-1 (1% GeO_2 by weight). The same process was completed using for 3 and 5% GeO_2, with the resulting composites referred to as G-3 and G-5, respectively. AC without the addition of GeO_2 was also prepared as a comparison to the three prepared composites and referred to as G-0.

2.3. Characterization. X-ray diffraction (XRD) patterns were collected using an X-ray diffractometer (Shimadzu 7000) equipped with a Cu Kα radiation source with a wavelength (λ) of 1.54 Å operated over a $20° \leq 2\theta \leq 70°$ range at 40 kV, 30 mA, with a step size 0.02°, at a scan rate of 2 min^{-1}. The size of the crystallites was calculated using the Scherrer equation as follows[11,33]

$$D = \frac{k\lambda}{\beta \cos\theta} \quad (1)$$

where D is the crystallite size (nm), k is the shape factor (the Scherrer constant), λ is the wavelength of the X-ray source (nm), β is full width half maximum (fwhm) value of a certain diffraction peak (in degrees), and θ is the Bragg angle. Fourier-transform infrared (FTIR) spectroscopy (IRPrestige-21, Shimadzu Corp) was used to identify the chemical bonds and functional groups of the synthesized composites in the range of 3700−300 cm^{-1}. UV−visible (UV−vis) spectroscopy (UV-1800 UV−vis spectrophotometer, Shimadzu) was used to determine the absorption ranges of the sample toward the MB and CR pollutants, which were then used to calculate the percentages of degradation, adsorption quantities, and kinetic analyses. Using UV−vis spectroscopy, the wavelength of the absorption edge of the catalyst can also be determined, which can then be used to calculate the bandgap energy value E_g using the following equation[11,34]

$$E_g = hc/\lambda \quad (2)$$

where E_g is the bandgap energy (eV), h is Planck's constant (4.1357×10^{-15} eV s), c is the speed of light (2.998×10^8 m/s), and λ is the wavelength of the sample absorption edge (nm).

2.4. Photodegradation Process. The photodegradation activities of G-0, G-1, G-3, and G-5 were evaluated using MB and CR under an optic lamp (halogen display, Germany). In the initial step, the MB solution (consisting of 10 mL of MB dissolved in 100 mL of distilled water) was placed in a 500 mL beaker, to which G-1 (0.1 g) was added. Furthermore, the mixture was stirred using a magnetic stirrer for 15 min and then covered and irradiated using the optic lamp. The mixture (10 mL) was taken up in a pipet every minute up to five times, then dripped into a funnel coated with filter paper (number 42), and then stored in a plastic bottle. The abovementioned procedure was repeated for catalysts G-0, G-3, and G-5.

As for CR, CR powder (0.04 g) was dissolved in distilled water (1000 mL). After stirring, CR solution (100 mL) was placed in a 500 mL beaker, followed by the addition of G-1 (0.1 g). The mixture was then subjected to the same treatment as the previous pollutant, with an irradiation time of 30 min, and a sample of the mixture was taken every 10 min. The same procedure was also conducted for catalysts G-0, G-3, and G-5. The percentage of pollutant degradation (D) was then calculated using the following equation[35]

$$D(\%) = \frac{C_0 - C_t}{C_0} \times 100\% \quad (3)$$

where C_0 is the initial concentration and C_t is the concentration after irradiation at time t.

3. RESULTS AND DISCUSSION

3.1. Structural Analysis. The crystal structures of the synthesized materials were analyzed by XRD, as the XRD patterns show in Figure 1a. The diffraction peaks at 2θ = 20−30° and 40−48° indicate that the AC has an amorphous structure, identified as carbon (002) and carbon (101).[36−38] As reported in literature,[38] the diffraction peaks arise because

https://doi.org/10.1021/acsomega.3c03526
ACS Omega 2023, 8, 27663−27673

the AC is made of graphite-like microcrystals, composed of several graphite-like layers spaced evenly at random orientations connected by a network of crosslinks.

In Figure 1b, the peak at 2θ = 26.9682° (G-0) can be observed to shift to 2θ = 26.8057° (G-5), followed by an increase in the fwhm value. Based on eq 1, the crystallite size is inversely proportional to the fwhm value, resulting in a decrease in crystal size after a peak shift occurs, which can be seen in Table 1. The new peak at 2θ = 26.1416° for catalyst G-5 is associated with the relationship between the matrix material (AC) and filler material (GeO_2). GeO_2, which successfully enters the AC lattice, will also be explained in the FTIR and UV−vis spectroscopy analysis.

Table 1. Value of the Interatomic Spacing (d-Spacing), fwhm, and Crystallite Size of G-0 and G-5 at 2θ

catalyst	2θ (deg)	d-spacing (Å)	fwhm (deg)	Crystallite size (nm)
G-0	26.9682	3.30520	0.3036	26.9087
G-5	26.8057	3.32318	0.3486	23.4272
	26.1416	3.40607	0.6167	13.2246

The chemical bonds were identified using FTIR spectroscopy from the spectra shown in Figure 1c. Based on the spectral analysis, the hydroxyl groups (−OH) at 3421 and 1024 cm^{-1} can be attributed to the activation of the carbon from the oxidizing agent.[38−40] At 2926 and 2376 cm^{-1}, C−H and C═O stretching occur, respectively, the presence of which can be attributed to the combustion residue still present in the catalyst.[39] A quinone-like structure with C═O stretching vibrations and a carboxylic acid group (−COOH) was identified at 1558 and 1400 cm^{-1}.[40,41] The peak at 779 cm^{-1} can be attributed to C−O−C, which increased in intensity with the addition of GeO_2.[42] As for the peak 570 cm^{-1}, this is related to covalent bonding such as that in Al_2O_3, which is contained in the amorphous AC (Beran et al., 2001).[43] The addition of GeO_2 forms a C−Ge−C bond, which presents a peak at 396 cm^{-1}, and there is an apparent expansion in Ge−C−Ge bonds in G-5.

3.2. Morphology Analysis. Scanning electron microscopy (SEM) was employed to analyze the inner structure and fracture shape of the composite by observing their surface morphology.[44] Figure 2 shows SEM images of G-0 and G-5, where various pore shapes can be observed on the surface of the AC, such as slit-shaped, cylindrical, and conical pores.[44] According to the reported literature,[44] there are four types of pores based on their connectivity, i.e., passing, interconnected, dead-end, and closed pores. The first three types of pores can be seen clearly in Figure 2a,b, while closed pores can be observed in Figure 2a′,b′. With reference to the literature,[45] the composite particles are irregularly composed of different sizes, resulting in the appearance of cavities and channels that are arranged randomly. A similar result was reported in ref 46 by using high resolution transmission electron microscopy, which presents the porous structure plane of the inner GeO_2 crystalline with agglomeration in the form of granules. The spherical and ellipsoid forms of the observed composites exhibit a high specific surface area, as reported in the literature,[45,47] which indicate that high numbers of active sites can be correlated to the adsorption ability of the composites. The shapes and surface states examined through TEM exhibit conformity with the findings presented in ref 48, wherein the shape configuration is covered by an amorphous phase, attributed to the existence of carbon. The desired GeO_2 crystals were acquired in white rounded mono-sized crystals on the surface of the AC, as reported in the literature,[49−51] which can be observed in Figure 2b.

For surface characterization and chemical state analysis to support morphology analysis can be provided by using X-ray photoelectron spectroscopy. A comprehensive and accurate understanding of the surface properties of G-1, G-3, and G-5 composite materials is necessary to effectively identify and regulate their photocatalytic performance. According to Table 2, the process of surface modification of catalysts is often linked to the investigation of adsorption and reaction phenomena, and it can be linked to the binding energy range for Ge and C state. This involves subjecting the catalysts to specific gases or liquids and analyzing the surface chemical

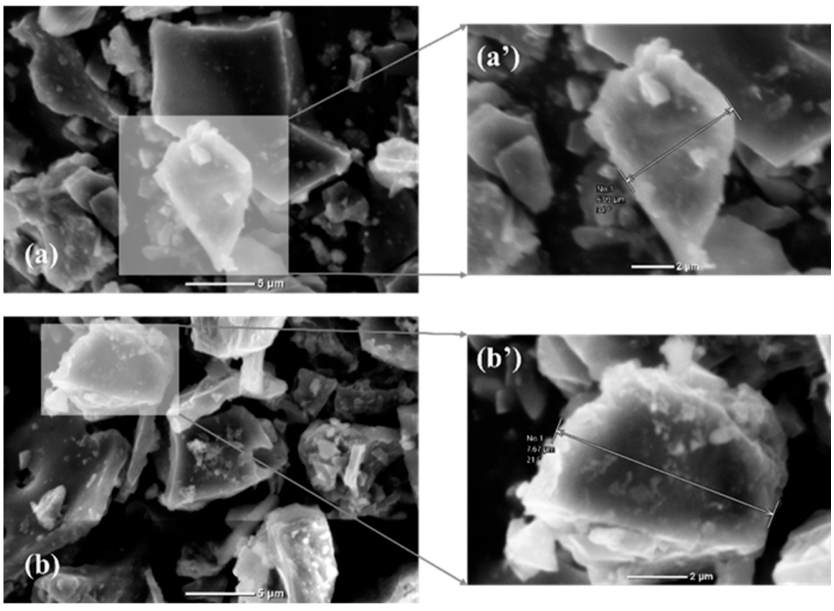

Figure 2. SEM images of (a) G-0 and (a′) corresponding magnified image of G-0 and (b) G-5 and (b′) its corresponding magnified image.

https://doi.org/10.1021/acsomega.3c03526
ACS Omega 2023, 8, 27663−27673

Table 2. Binding Energy and Chemical State from Several Previous Studies for GeO_2 and C

materials	binding energy (eV)	chemical state	refs
GeO_2	1252	(GeO) $2p_{1/2}$	53
	1221	($Ge^{\bullet\bullet}$) $2p_{1/2}$	
GeO_2	32.5	(GeO_2) $2p_{5/2}$	52
GeO_2	30	Ge 3d	54
$Gd_5Ge_2Si_2$ doped Co	27.6	Ge $3d^5$	55
C	284.7	(C=C) sp^2	56−58
C	285.3	(C−C) sp^3	59−61
C	288.4	C−O−C	62−65

state. The formation of C−C, C=C, and C−O−C bonds in 284−288 eV and the oxygen-containing bonds in GeO_2 is facilitated by the presence of edge and defect sites, which serve as appropriate anchoring sites for the functionalities involved in the generation of singlet oxygen ($^{\bullet}O_2$) and hydroxil ions (−OH). The non-bridging electron pairs that are not involved in bonding are located on the germanium atom that has a coordination number of two. This is symbolized as $Ge^{\bullet\bullet}$, where the symbol (=) represents the bonds with two oxygen atoms and ($\bullet\bullet$) denotes the presence of a lone electron pair.[52,53] Through this approach, it is possible to detect the formation of reaction intermediates or by-products during the photocatalytic process.

3.3. UV Analysis. The optical properties of the composites were analyzed by UV−vis spectroscopy, with the results shown in Figure 3a,b for the MB and CR pollutants, respectively. MB absorption occurs at a wavelength of 550−700 nm, which indicates that the sample successfully absorbed MB. The results correspond to the literature,[66] which has an absorption area at a wavelength of 500−700 nm. As for CR, the absorption occurs at a wavelength of 450−550 nm. Based on literature,[67] CR absorption occurs at a wavelength of 497 nm. These results indicate that the samples will be effective across the entire visible light region (400−700 nm).

The bandgap energy was calculated using eq 2 with the calculation results shown in Table 3. The E_g values of the catalysts are below the E_g value of AC of 4.5 eV,[37] with values of 4.14, 4.04, and 4.16 eV calculated for G-1, G-3, and G-5,

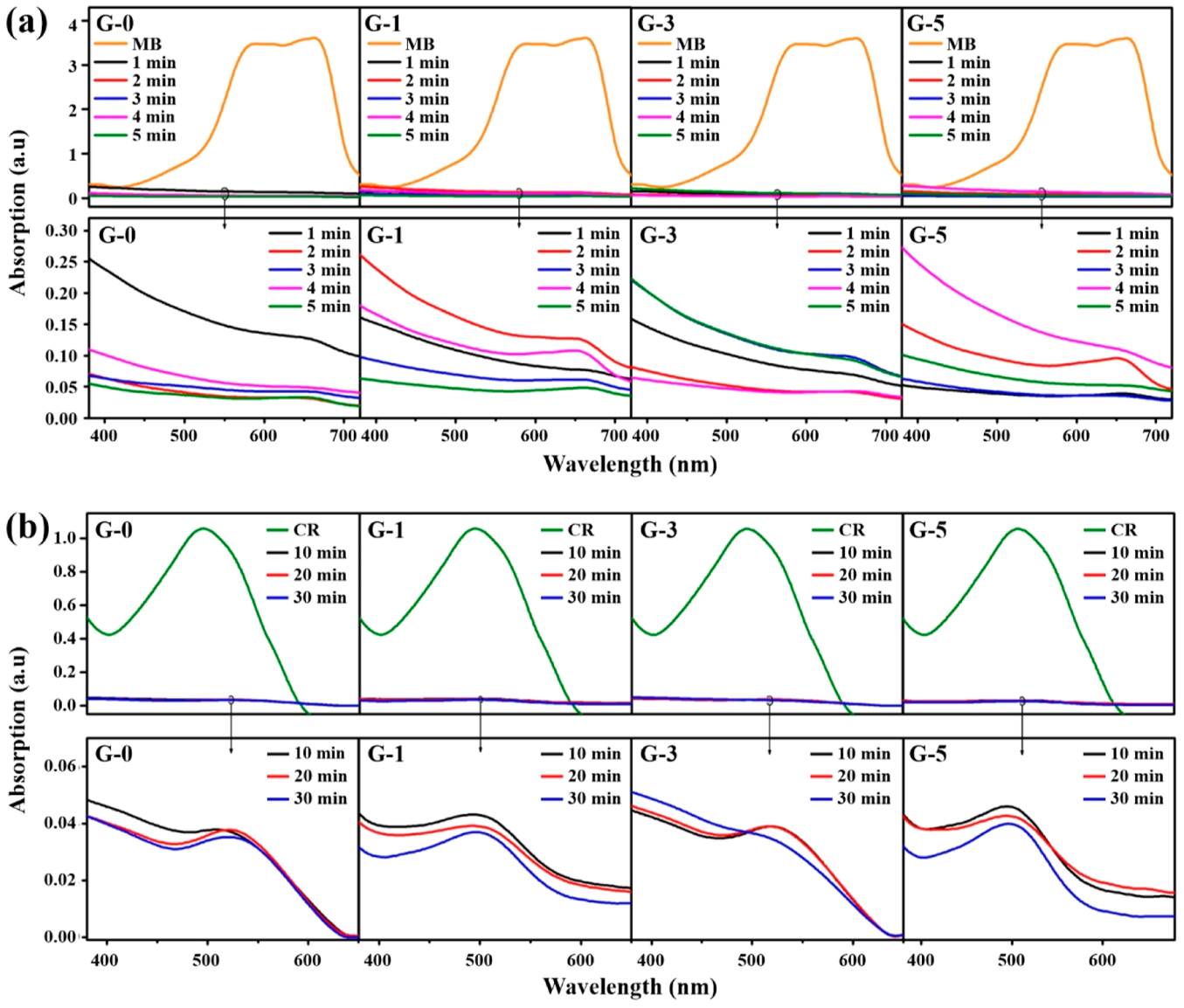

Figure 3. UV−vis spectra of (a) MB in the wavelength range of 380−720 nm and (b) CR in the wavelength range of 380−680 nm.

https://doi.org/10.1021/acsomega.3c03526
ACS Omega 2023, 8, 27663−27673

Table 3. Bandgap Energy and the Absorption Edge Wavelength of the Catalysts

catalyst	absorption edge wavelength (nm)	bandgap energy (eV)
GeO_2	314	3.94
G-1	299	4.14
G-3	307	4.04
G-5	298	4.16

respectively. The decrease in the bandgap energy of AC when 1, 3, and 5% GeO_2 was added indicates that GeO_2 enters the AC lattice.[68] This result is also related to the band gap domain combination from the material of origin as reported by ref 69 for AC ∼2.2 eV and ref 70 for GeO_2 ∼ 4.6 eV. A composite band gap of approximately ∼4 eV can be declared reasonable based on the previously mentioned band gaps.

3.4. Photocatalytic Activity. Based on the results shown in Figure 3a,b, photoreduction occurs in the visible light range. AC with added GeO_2 shows almost the same degradation performance as AC without the addition of GeO_2, which can be seen in Table 4, and the photocatalytic performance during irradiation can be seen in Figure 4a,b. The degradation percentage values were close to each other due to the addition of relatively small amounts of GeO_2, namely 1, 3, and 5% of the total quantity of AC. Therefore, for MB, the catalyst with the best degradation percentage was G-0. The excellent performance of AC in degrading MB is due to the absorption region of AC being the same as that of MB, namely, 500−700 nm for AC and 557−699 nm for MB.[71] The same results were also reported in the literature,[72] where AC was shown to degrade under visible light in the wavelength range of 550−680 nm. As for the CR pollutant, the catalyst with the best degradation percentage was G-5 as the addition of GeO_2 into AC extends the absorption spectrum to the lower wavelength region. It is possible that with the addition of GeO_2, the catalyst will approach the UV region in terms of its absorbance. The highest photodegradation efficiency observed in this study was compared to other studies employing MB and CR as the pollutants, testing various irradiation times and photocatalyst loading, with the results listed in Table 5. This corresponds to the value of the wavelength of the GeO_2 absorption edge, which is 314 nm (Table 3), which means that GeO_2 can absorb in the UV region. The location of the CR absorption region, which is in the wavelength range of 497 nm,[67] makes G-5 the catalyst that works the best in degrading CR pollutants.

3.5. Adsorption Quantity. The adsorption process aims to separate contaminants from MB and CR waste. Figure 4c,d shows a graph of the adsorption quantity versus the irradiation time for MB (10 mL/100 mL) and CR (40 mg/1000 mL). The adsorption quantity was calculated using the following equations[77]

$$Q_{ads} = (C_0 - C_t)\cdot V/m \quad (4)$$

where Q_{ads} (mg g^{-1}) is the adsorbed quantity at time t, C_0 is the initial concentration (mg L^{-1}), C_t is the concentration (mg L^{-1}) at time t of adsorption process, V is the volume of dye solution (L), and m is the mass (g) of the catalyst. These values are shown in Table 6.

The adsorption quantity values increased with the increasing irradiation time of the pollutants. Even though the amount of the catalyst put into each waste solution was only 0.1 g, it was clear that the catalyst could still function well. The G-0 catalyst exhibited the highest adsorption of MB after 5 min of irradiation. As for CR, after 30 min of irradiation, G-5 showed the highest adsorption. The difference in adsorption quantity between the MB and CR pollutants is caused by differences in catalyst composition that are optimal for each pollutant. The composition of AC in the catalyst that showed the best performance toward MB was 100%, so the quantity of adsorption obtained was high. As for the CR pollutant, the catalyst composition with the best performance was a catalyst with a composition of 5% GeO_2 and 95% AC. The relatively low amount of GeO_2 affects the quantity of adsorbed CR, which is consistent with the previous explanation that the presence of GeO_2 affects the ability of the catalyst to degrade CR. The adsorption equilibrium state for MB and CR pollutants was yet to be reached in the experiments. It is estimated that the irradiation time for each pollutant to reach an equilibrium point will take longer, as in a literature study,[72] where it was reported that to reach this point is takes 70 min for MB pollutants and 90 min for CR.[78]

3.6. Kinetic Analysis. The kinetics of the adsorption process can be stated by the Langmuir equation,[79−81] with a new transformation which shows a hybrid rate equation[80−82]

$$\frac{dq_t}{dt} = k_1(q_e - q_t) + k_2(q_e - q_t)^2 \quad (5)$$

with

$$k_1 = [k_a^2(C_0 - q_{max}X)^2 + 2k_ak_d(C_0 + q_{max}X) + k_d^2]^{1/2} \quad (6)$$

$$k_2 = k_aq_{max}X \quad (7)$$

where q_t is the adsorption amount of adsorbent at time t, and q_e and q_{max} are the adsorption amounts of adsorbent at equilibrium and maximum capacity, respectively. k_a and k_d are the adsorption and desorption rate constant, respectively. C_0 is the initial adsorbate concentration, and X is the dosage of adsorbent. It is stated in the literature[80] that eq 1 can be reduced into first- and second-order rate equations under certain conditions, which are:

(i) If $k_1 \gg k_2(q_e - q_t)$, eq 1 reduces to a first-order rate equation that has the same form as the Lagergren

Table 4. Percentage of Degradation of G-0, G-1, G-3, and G-5 for MB and CR Pollutants

catalyst	% degradation of MB with time (min)					% degradation of CR with time (min)		
	1	2	3	4	5	10	20	30
G-0	95.50	98.62	98.81	99.06	99.09	96.58	96.82	96.97
G-1	96.45	96.97	97.88	98.26	98.62	96.02	96.39	96.61
G-3	97.27	97.44	98.04	98.79	98.84	96.55	96.59	96.60
G-5	96.92	97.22	98.51	98.87	98.98	96.99	97.21	97.41

https://doi.org/10.1021/acsomega.3c03526
ACS Omega 2023, 8, 27663−27673

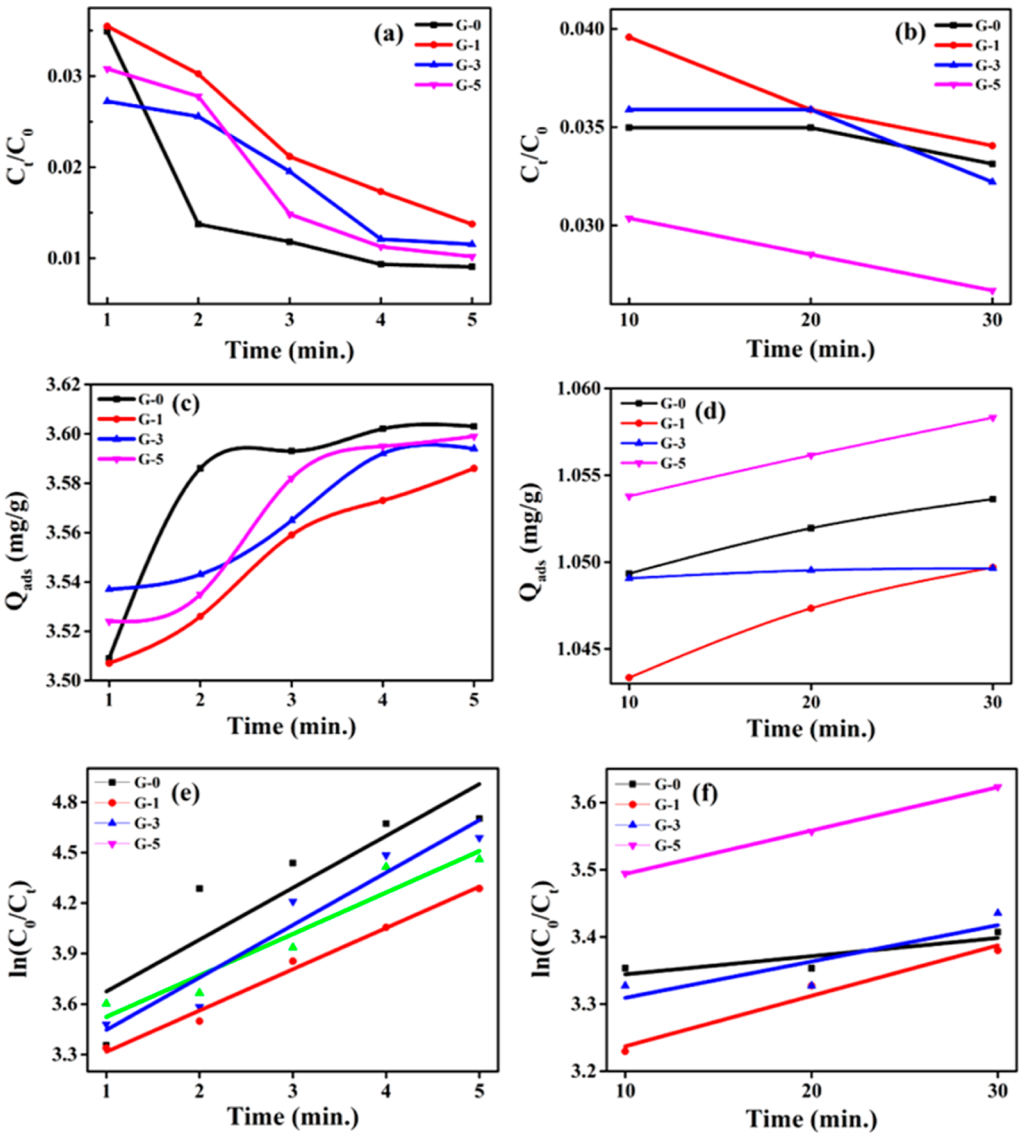

Figure 4. Rate removal of (a) MB and (b) CR; adsorption quantity of (c) MB and (d) CR; pseudo-first order kinetics curve of (e) MB and (f) CR.

Table 5. Comparison of the Photocatalytic Activities of Previous Published Literature for Comparison with That of the AC/GeO_2 Composite in This Study

catalyst	catalyst loading (g/L)	pollutant	highest degradation (%), time	refs
Co−Ox−ACs	0.1	MB	98%, 60 min	73
Ni−Ox−ACs	0.1		91%, 60 min	
TiO_2/CSAC(2:1)	0.1	MB	100%, 80 min	74
H_3PO_4 as an activator/egg shell as AC(4:1)	0.5	MB	83%, 120 min	71
FDT/PAC	0.06	CR	100%, 60 min	75
WO_3−TiO_2/AC	10	CR	95.21%, 120 min	76
AC	0.1	MB	99.09%, 5 min	present study
AC/GeO_2	0.1	CR	97.41%, 30 min	

equation, i.e., pseudo-first-order (PFO) rate equation[80,81,83]

Table 6. Reaction Rate Constants (k_1) and Correlation Coefficient Values (R^2) of the Photocatalytic Degradation of MB and CR

samples	MB		CR	
	rate constant (k_1)(min−1)	correlation coefficient values (R^2)	rate constant (k_1) (min−1)	correlation coefficient values (R^2)
G-0	0.3081	0.7826	0.0027	0.7500
G-1	0.2453	0.9886	0.0075	0.9710
G-3	0.2463	0.9253	0.0054	0.7500
G-5	0.3117	0.9301	0.0065	0.9997

$$\frac{dq_t}{dt} = k_1(q_e - q_t) \tag{8}$$

When eq 4 was integrated with the boundary conditions $t = 0$ to $t = t$ and $q_t = 0$ to $q_t = q_t$, the following equation can be obtained[81,83]

$$\ln\frac{(q_e - q_t)}{q_e} = -k_1 t \tag{9}$$

https://doi.org/10.1021/acsomega.3c03526
ACS Omega 2023, 8, 27663−27673

where k_1 is the PFO rate constant. By plotting $\ln(q_e - q_t)$ vs t, a linearized model of the adsorption process can be obtained, with $k_1 = -m$, and $q_e = \exp(b)$, with m = slope and b = intercept.[81]

(ii) If $k_1 \ll k_2(q_e - q_t)$, eq 1 takes the form of a second-order rate equation, known as a pseudo-second-order (PSO) rate equation[80,81,83,84]

$$\frac{dq_t}{dt} = k_2(q_e - q_t)^2 \quad (10)$$

(iii) Integrating eq 6 with the boundary conditions $t = 0$ to $t = t$ and $q_t = 0$ to $q_t = q_t$, the following expression can be obtained[81,83]

$$\frac{1}{(q_e - q_t)} = \frac{1}{q_e} + k_2 t \quad (11)$$

and by adjusting eq 7 to obtain a linearized form, the following equation is obtained[81,83]

$$\frac{t}{q_t} = \left(\frac{1}{q_e}\right)t + \frac{1}{k_2 q_e^2} \quad (12)$$

where k_2 is the rate constant of PSO. By plotting $\frac{t}{q_t}$ vs t, a linear fit of the adsorption process can be obtained, with $k_2 = \frac{m^2}{b}$ and $q_e = m^{-1}$.[81]

The correlation coefficient (R^2) is defined as follows[81,85,86]

$$R^2 = 1 - \frac{\sum_{i=1}^{n}(y_i - \hat{y}_i)^2}{\sum_{i=1}^{n}(y_i - \bar{y})^2} \quad (13)$$

where y_i is the experimental response at ith observation, $\hat{y}_i$ and $\bar{y}$ are the calculated and average value of y_i, respectively, and n is the number of observations. In this study, the catalysts were investigated using a PFO rate equation,[80,81,83] as shown in Figure 4e,f, with k_1 and R^2 values listed in Table 6. Using the correlation coefficient values, the fit accuracies can be measured.[81,85,86] As reported in the literature,[85] most cases where a PSO is applied as the rate model had data at equilibrium, resulting in a superior fit ($R^2 = 1$) since $\frac{t}{q_t} = \frac{t}{q_e}$. Meanwhile, for PFO cases, when q_t approaches q_e, the value of $(q_e - q_t)$ decreases; consequently, $\ln(q_e - q_t)$ increases. This phenomenon reduces the accuracy of PFO. Therefore, using the same function, i.e., eq 13, to calculate R^2 for both PFO and PSO cases is paramount.

3.7. Recyclability of the Synthesized Composites. The future prospects and applicability of any newly designed photocatalytic framework fully depend on their recyclability and stability. Therefore, all the synthesized materials were used for three consecutive photocatalytic reactions in the removal of MB, with the results shown in Figure 5. After the first cycle, the catalysts were recovered by centrifugation, washed three times with aquades, and dried at 90 °C for 40 min. The dried catalysts were then used in the second cycle of the reaction under irradiation. The same method was used for the third reaction, with each reaction lasting 5 min. The results showed a 5−9% reduction in the degradation rate by the end of the third cycle, which might be due to the loss of photocatalytic material during the washing and separation process of photocatalyst for its further use. The highly acceptable performance of the newly designed photocatalyst thus opens up new avenue toward its utilization in various environmental-related applications.

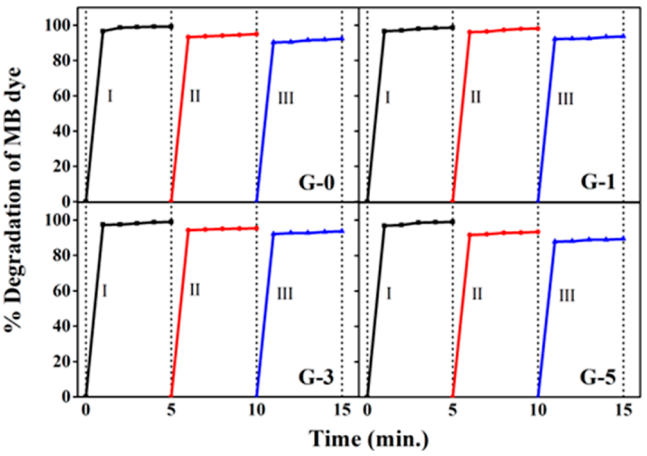

Figure 5. Recyclability of the synthesized catalysts for the removal of MB under visible light.

3.8. Photocatalytic Mechanism. A photocatalytic mechanism for the degradation of MB is shown in Figure 6. As illustrated, the photocatalytic process begins with the presence of photons on the surface of the photocatalyst material under visible light, followed by the transfer of energy from these photons to the VB of AC/GeO_2. If the energy transferred by the photons is greater than or equal to the energy gap between the upper VB and the lower CB then the e^- charges in the VB will be excited to the CB. The excited e^- then leaves a h^+ in the VB. Therefore, e^-−h^+ pairs are generated via this process.[87] The h^+ left in the VB thus have a sufficient lifetime to promote a redox reaction to achieve the degradation of the pollutants. Meanwhile, the stabilized e^- react with the dissolved oxygen (O_2) in the solution and generate active O_2^- radicals that degrade the pollutants into small molecules and finally harmless product. In energy transfer process, singlet oxygen ($^{\bullet}O_2$) is generated through the process of energy transfer from the excited photocatalyst to molecular oxygen (O_2). Singlet oxygen can directly oxidize organic pollutants. The high oxidation potential and short lifespan of this substance result in the degradation of organic compounds. Besides that, oxidative agents such as the hydroxyl radical exhibit potent and highly reactive properties. The photocatalyst facilitates a reaction between photogenerated holes (h^+) and either water molecules or hydroxide ions (OH^-). The hydroxyl radical facilitates the oxidation of organic pollutants, leading to the formation of smaller and comparatively less hazardous molecules. The presence of an unpaired electron renders it highly reactive and susceptible to oxidation.

4. CONCLUSIONS

In this study, AC/GeO_2 was successfully synthesized using the sol−gel method. The resulting AC/GeO_2 has an amorphous structure and absorbs in the visible light region. Moreover, the composites G-0 and G-5 exhibited highly favorable results in terms of their effectiveness toward MB and CR, as evidenced by their respective removal percentages of 99.09 and 97.41%. In addition, the composite shows high reusability, as seen in the percentage of catalyst degradation, which is still above >90% after three cycles. The photocatalysts that were synthesized exhibit considerable photocatalytic activity,

https://doi.org/10.1021/acsomega.3c03526
ACS Omega 2023, 8, 27663−27673

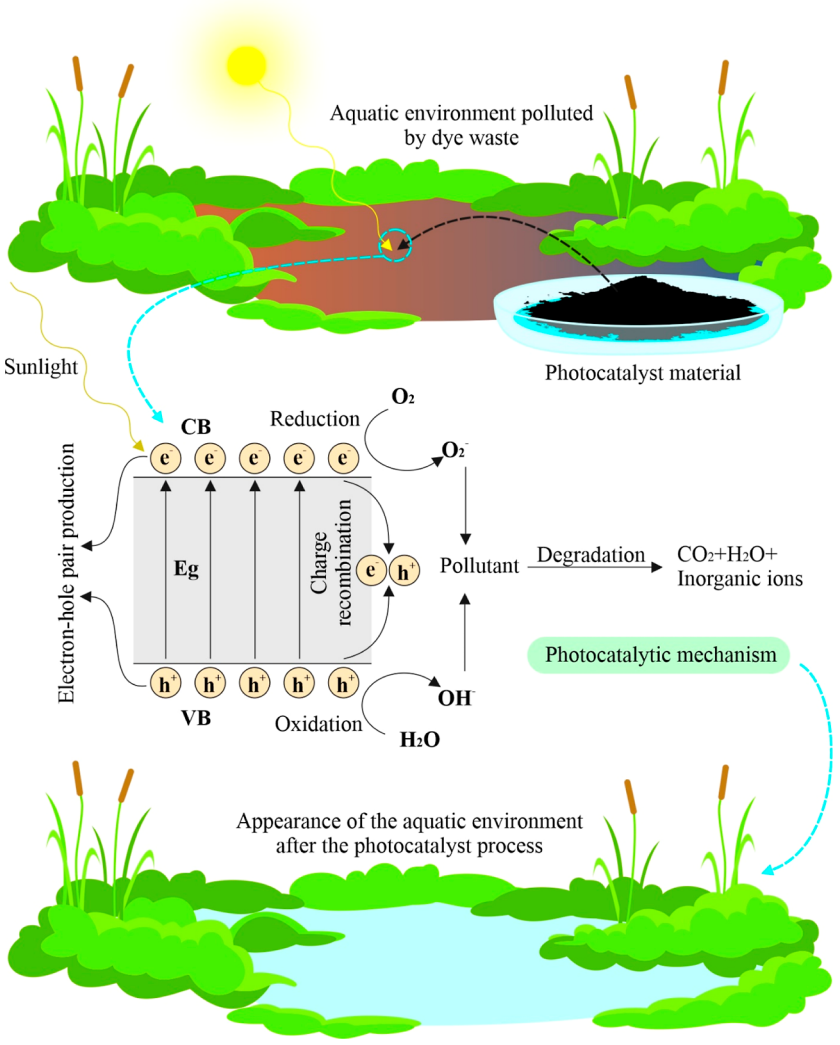

Figure 6. Schematic representation of the mechanism of the photocatalytic process.

rendering them viable for employment in the remediation of groundwater contaminants with a high degree of efficacy. The adsorption of MB and CR exhibited an increase in proportion to the duration of irradiation, with the maximum adsorption capacity for each contaminant being 3.603 and 1.0583 mg/g, respectively. Adsorption kinetics were modeled using a first-order Langmuir process, showing that the catalyst reasonably adhered to the PFO model.

AUTHOR INFORMATION

Corresponding Author

Dahlang Tahir − *Department of Physics, Hasanuddin University, Makassar 90245, Indonesia;* orcid.org/0000-0002-8241-3604; Phone: +62-411-587634; Email: dtahir@fmipa.unhas.ac.id

Authors

Yulia Fajriani − *Department of Physics, Hasanuddin University, Makassar 90245, Indonesia*

Heryanto Heryanto − *Department of Physics, Hasanuddin University, Makassar 90245, Indonesia*

Complete contact information is available at: https://pubs.acs.org/10.1021/acsomega.3c03526

Author Contributions

Yulia Fajriani: Writing, illustration, and editing—original draft. Heryanto Heryanto: Software, validation, and writing—original draft. Dahlang Tahir: Writing—original draft, editing, review, and finalization.

Notes

The authors declare no competing financial interest.

All data and materials generated or analyzed during this study are included in this article.

ACKNOWLEDGMENTS

Thanks for valuable discussion member of Material and Energy Laboratory, Department of Physics, Hasanuddin University, Indonesia.

REFERENCES

(1) Zhang, P.; Liao, Q.; Yao, H.; Huang, Y.; Cheng, H.; Qu, L. Direct Solar Steam Generation System for Clean Water Production. *Energy Storage Mater.* **2019**, *18*, 429−446.

(2) Mueller, J. T.; Gasteyer, S. The Widespread and Unjust Drinking Water and Clean Water Crisis in the United States. *Nat. Commun.* **2021**, *12*, 3544.

(3) van Vliet, M. T. H.; Jones, E. R.; Flörke, M.; Franssen, W. H. P.; Hanasaki, N.; Wada, Y.; Yearsley, J. R. Global Water Scarcity

https://doi.org/10.1021/acsomega.3c03526
ACS Omega 2023, 8, 27663−27673

Including Surface Water Quality and Expansions of Clean Water Technologies. *Environ. Res. Lett.* **2021**, *16*, 024020.
(4) Jury, W. A.; Vaux, H. J. The Emerging Global Water Crisis: Managing Scarcity and Conflict Between Water Users. *Adv. Agron.* **2007**, *95*, 1−76.
(5) Mehta, P. Impending Water Crisis in India and Comparing Clean Water Standards among Developing and Developed Nations. *Arch. Appl. Sci. Res.* **2012**, *4*, (1) 497−507.
(6) Rosa, L.; Chiarelli, D. D.; Rulli, M. C.; Dell'angelo, J.; D'Odorico, P. Global Agricultural Economic Water Scarcity. *Sci.Adv.* **2020**, *6*, No. eaaz6031.
(7) Ma, T.; Sun, S.; Fu, G.; Hall, J. W.; Ni, Y.; He, L.; Yi, J.; Zhao, N.; Du, Y.; Pei, T.; Cheng, W.; Song, C.; Fang, C.; Zhou, C. Pollution Exacerbates China's Water Scarcity and Its Regional Inequality. *Nat. Commun.* **2020**, *11*, 650.
(8) Boretti, A.; Rosa, L. Reassessing the Projections of the World Water Development Report. *npj Clean Water* **2019**, *2*, 15.
(9) Donkadokula, N. Y.; Kola, A. K.; Naz, I.; Saroj, D. A Review on Advanced Physico-Chemical and Biological Textile Dye Wastewater Treatment Techniques. *Rev. Environ. Sci. Biotechnol.* **2020**, *19*, 543−560.
(10) Jo, W. K.; Tayade, R. J. Recent Developments in Photocatalytic Dye Degradation upon Irradiation with Energy-Efficient Light Emitting Diodes. *J. Catal.* **2014**, *35*, 1781−1792.
(11) Natarajan, K.; Bajaj, H. C.; Tayade, R. J. Direct Sunlight Driven Photocatalytic Activity of GeO2/Monoclinic-BiVO4 Nanoplate Composites. *Sol. Energy* **2017**, *148*, 87−97.
(12) Hussain, T.; Wahab, A. A Critical Review of the Current Water Conservation Practices in Textile Wet Processing. *J. Cleaner Prod.* **2018**, *198*, 806−819.
(13) Lellis, B.; Fávaro-Polonio, C. Z.; Pamphile, J. A.; Polonio, J. C. Effects of Textile Dyes on Health and the Environment and Bioremediation Potential of Living Organisms. *Biotechnol. Res. Innov.* **2019**, *3*, 275−290.
(14) Nageeb, M. Adsorption Technique for the Removal of Organic Pollutants from Water and Wastewater. In *Organic Pollutants—Monitoring, Risk and Treatment*; InTech, 2013. DOI: 10.5772/54048.
(15) Deng, Y.; Zhao, R. Advanced Oxidation Processes (AOPs) in Wastewater Treatment. *Curr. Pollut. Rep.* **2015**, *1*, 167−176.
(16) Chan, S. H. S.; Yeong Wu, T.; Juan, J. C.; Teh, C. Y. Recent Developments of Metal Oxide Semiconductors as Photocatalysts in Advanced Oxidation Processes (AOPs) for Treatment of Dye Waste-Water. *J. Chem. Technol. Biotechnol.* **2011**, *86*, 1130−1158.
(17) Xu, Q.; Zhang, L.; Cheng, B.; Fan, J.; Yu, J. S-Scheme Heterojunction Photocatalyst. *Chem* **2020**, *6*, 1543−1559.
(18) Ameta, R.; Solanki, M. S.; Benjamin, S.; Ameta, S. C. Photocatalysis. In *Advanced Oxidation Processes for Wastewater Treatment: Emerging Green Chemical Technology*; Elsevier Inc., 2018; pp 135−175. DOI: 10.1016/B978-0-12-810499-6.00006-1.
(19) Song, C.; Wang, L. J.; Sun, S. M.; Wu, Y.; Xu, L. J.; Gan, L. Preparation of Visible-Light Photocatalysts of Bi2O3/Bi Embedded in Porous Carbon from Bi-Based Metal Organic Frameworks for Highly Efficient Rhodamine B Removal from Water. *New Carbon Mater.* **2020**, *35*, 609−618.
(20) Martins, A. C.; Cazetta, A. L.; Pezoti, O.; Souza, J. R. B.; Zhang, T.; Pilau, E. J.; Asefa, T.; Almeida, V. C. Sol-Gel Synthesis of New TiO2/Activated Carbon Photocatalyst and Its Application for Degradation of Tetracycline. *Ceram. Int.* **2017**, *43*, 4411−4418.
(21) Andriantsiferana, C.; Mohamed, E. F.; Delmas, H. Photo-catalytic Degradation of an Azo-Dye on TiO2/Activated Carbon Composite Material. *Environ. Technol.* **2014**, *35*, 355−363.
(22) Shi, J. W.; Cui, H. J.; Chen, J. W.; Fu, M. L.; Xu, B.; Luo, H. Y.; Ye, Z. L. TiO 2/Activated Carbon Fibers Photocatalyst: Effects of Coating Procedures on the Microstructure, Adhesion Property, and Photocatalytic Ability. *J. Colloid Interface Sci.* **2012**, *388*, 201−208.
(23) Asiltürk, M.; Şener, Ş. TiO 2-Activated Carbon Photocatalysts: Preparation, Characterization and Photocatalytic Activities. *Chem. Eng. J.* **2012**, *180*, 354−363.
(24) Sobana, N.; Swaminathan, M. Combination Effect of ZnO and Activated Carbon for Solar Assisted Photocatalytic Degradation of Direct Blue 53. *Sol. Energy Mater. Sol. Cells* **2007**, *91*, 727−734.
(25) Muthirulan, P.; Meenakshisundararam, M.; Kannan, N. Beneficial Role of ZnO Photocatalyst Supported with Porous Activated Carbon for the Mineralization of Alizarin Cyanin Green Dye in Aqueous Solution. *J. Adv. Res.* **2013**, *4*, 479−484.
(26) Chen, X.; Wu, Z.; Gao, Z.; Ye, B. C. Effect of Different Activated Carbon as Carrier on the Photocatalytic Activity of Ag-N-ZnO Photocatalyst for Methyl Orange Degradation under Visible Light Irradiation. *Nanomaterials* **2017**, *7*, 258.
(27) Raizada, P.; Singh, P.; Kumar, A.; Sharma, G.; Pare, B.; Jonnalagadda, S. B.; Thakur, P. Solar Photocatalytic Activity of Nano-ZnO Supported on Activatedcarbon or Brick Grain Particles: Role of Adsorption in Dye Degradation. *Appl. Catal., A* **2014**, *486*, 159−169.
(28) Le, S.; Jiang, T.; Li, Y.; Zhao, Q.; Li, Y.; Fang, W.; Gong, M. Highly Efficient Visible-Light-Driven Mesoporous Graphitic Carbon Nitride/ZnO Nanocomposite Photocatalysts. *Appl. Catal., B* **2017**, *200*, 601−610.
(29) Scaria, J.; Karim, A. v.; Divyapriya, G.; Nidheesh, P. v.; Suresh Kumar, M. Carbon-Supported Semiconductor Nanoparticles as Effective Photocatalysts for Water and Wastewater Treatment. In *Nano-Materials as Photocatalysts for Degradation of Environmental Pollutants: Challenges and Possibilities*; Elsevier, 2019; pp 245−278. DOI: DOI: 10.1016/B978-0-12-818598-8.00013-4.
(30) Natarajan, K.; Bajaj, H. C.; Tayade, R. J. Effective Removal of Organic Pollutants Using GeO2/TiO2 Nanoparticle Composites under Direct Sunlight. *Mater. Chem. Front.* **2018**, *2*, 741−751.
(31) Shinde, S. L.; Nanda, K. K. Photon-Free Degradation of Dyes by Ge/GeO 2 Porous Microstructures. *ACS Sustainable Chem. Eng.* **2019**, *7*, 6611−6618.
(32) Tahir, D.; Ilyas, S.; Abdullah, B.; Armynah, B.; Kang, H. J. Electronic Properties of Composite Iron (II, III) Oxide (Fe3O4) Carbonaceous Absorber Materials by Electron Spectroscopy. *J. Electron Spectrosc. Relat. Phenom.* **2018**, *229*, 47−51.
(33) Heryanto, H.; Tahir, D. The Correlations between Structural and Optical Properties of Magnetite Nanoparticles Synthesised from Natural Iron Sand. *Ceram. Int.* **2021**, *47*, 16820−16827.
(34) Amir, N.; Tahir, D.; Heryanto, H. Synthesis, Structural and Optical Characteristics of Fe3O4/Activated Carbon Photocatalysts to Adsorb Pesticide Waste. *J. Mater. Sci.: Mater. Electron.* **2023**, *34*, 445.
(35) Chen, L.; TranT, T.; Huang, C.; Li, J.; Yuan, L.; Cai, Q. Synthesis and Photocatalytic Application of Au/Ag Nanoparticle-Sensitized ZnO Films. *Appl. Surf. Sci.* **2013**, *273*, 82−88.
(36) Liu, X. Y.; Huang, M.; Ma, H. L.; Zhang, Z. Q.; Gao, J. M.; Zhu, Y. L.; Han, X. J.; Guo, X. Y. Preparation of a Carbon-Based Solid Acid Catalyst by Sulfonating Activated Carbon in a Chemical Reduction Process. *Molecules* **2010**, *15*, 7188−7196.
(37) Tahir, D.; Ilyas, S.; Abdullah, B.; Armynah, B.; Kim, K.; Kang, H. J. Modification in Electronic, Structural, and Magnetic Properties Based on Composition of Composites Copper (II) Oxide (CuO) and Carbonaceous Material. *Mater. Res. Express* **2018**, *6*, 035705.
(38) Hashemian, S.; Salari, K.; Yazdi, Z. A. Preparation of Activated Carbon from Agricultural Wastes (Almond Shell and Orange Peel) for Adsorption of 2-Pic from Aqueous Solution. *J. Ind. Eng. Chem.* **2014**, *20*, 1892−1900.
(39) Fanning, P. E.; Vannke, M. A. A DRIFTS Study of the Formation of Surface Groups on Carbon by Oxidation. *Carbon* **1993**, *31*, 721.
(40) He, Q.; Xu, Y.; Wang, C.; She, S.; Zhou, S.; Wang, R. Silane Modification and Characterization of Activated Carbon. *Adsorption* **2012**, *18*, 23−29.
(41) Lota, G.; Krawczyk, P.; Lota, K.; Sierczyńska, A.; Kolanowski, Ł.; Baraniak, M.; Buchwald, T. The Application of Activated Carbon Modified by Ozone Treatment for Energy Storage. *J. Solid State Electrochem.* **2016**, *20*, 2857−2864.
(42) Szumera, M.; Wacławska, I.; Mozgawa, W.; Sitarz, M. Spectroscopic Study of Biologically Active Glasses. *J. Mol. Struct.* **2005**, *744*−*747*, 609−614.

https://doi.org/10.1021/acsomega.3c03526
ACS Omega 2023, 8, 27663−27673

(43) Beran, A.; Voll, D.; Schneider, H. Dehydration and Structural Development of Mullite Precursors: An FTIR Spectroscopic Study. *J Eur. Ceram. Soc.* **2001**, *21* (14), 2479−2485.
(44) Nie, B.; Liu, X.; Yang, L.; Meng, J.; Li, X. Pore Structure Characterization of Different Rank Coals Using Gas Adsorption and Scanning Electron Microscopy. *Fuel* **2015**, *158*, 908−917.
(45) Bouhcain, B.; Mansouri, F. E.; Brigui, J.; Ruiz, S. G.; Alonso, J. M. Q.; Dekkaki, H. C.; Zerrouk, M. H. Study of Elimination of Emerging Contaminants by Adsorption Using Activated Carbon of Coconut (Amoxicillin−Penicillin−Theobromine). In *AIP Conference Proceedings*; American Institute of Physics Inc., 2021; Vol. *2417*,. DOI: 10.1063/5.0072592.
(46) Yan, S.; Song, H.; Lin, S.; Wu, H.; Shi, Y.; Yao, J. GeO $_2$ Encapsulated Ge Nanostructure with Enhanced Lithium-Storage Properties. *Adv. Funct. Mater.* **2019**, *29*, 1807946.
(47) Maroof, M. A.; Mahboubi, A.; Noorzad, A.; Safi, Y. A New Approach to Particle Shape Classification of Granular Materials. *Transp. Geotech.* **2020**, *22*, 100296.
(48) Seng, K. H.; Park, M.; Guo, Z. P.; Liu, H. K.; Cho, J. Catalytic Role of Ge in Highly Reversible GeO $_2$/Ge/C Nanocomposite Anode Material for Lithium Batteries. *Nano Lett.* **2013**, *13*, 1230−1236.
(49) Wysokowski, M.; Motylenko, M.; Beyer, J.; Makarova, A.; Stöcker, H.; Walter, J.; Galli, R.; Kaiser, S.; Vyalikh, D.; Bazhenov, V. v.; Petrenko, I.; Stelling, A. L.; Molodtsov, S. L.; Stawski, D.; Kurzydłowski, K. J.; Langer, E.; Tsurkan, M. v.; Jesionowski, T.; Heitmann, J.; Meyer, D. C.; Ehrlich, H. Extreme Biomimetic Approach for Developing Novel Chitin-GeO2 Nanocomposites with Photoluminescent Properties. *Nano Res.* **2015**, *8*, 2288−2301.
(50) Ramana, C. v.; Carbajal-Franco, G.; Vemuri, R. S.; Troitskaia, I. B.; Gromilov, S. A.; Atuchin, V. v. Optical properties and thermal stability of germanium oxide (GeO2) nanocrystals with α-quartz structure. *Mater. Sci. Eng., B* **2010**, *174*, 279−284.
(51) Atuchin, V. v.; Gavrilova, T. A.; Gromilov, S. A.; Kostrovsky, V. G.; Pokrovsky, L. D.; Troitskaia, I. B.; Vemuri, R. S.; Carbajal-Franco, G.; Ramana, C. v. Low-Temperature Chemical Synthesis and Microstructure Analysis of GeO_2 Crystals with α-Quartz Structure. *Cryst. Growth Des.* **2009**, *9*, 1829−1832.
(52) Harshavardhan Reddy, P.; Kir'yanov, A. V.; Dhar, A.; Das, S.; Dutta, D.; Pal, M.; Barmenkov, Y. O.; Minguella-Gallardo, J. A.; Bhadra, S. K.; Paul, M. C. Fabrication of Ultra-High Numerical Aperture GeO_2-Doped Fiber and Its Use for Broadband Supercontinuum Generation. *Appl. Opt.* **2017**, *56*, 9315.
(53) Almuslem, A. S.; Hanna, A. N.; Yapici, T.; Wehbe, N.; Diallo, E. M.; Kutbee, A. T.; Bahabry, R. R.; Hussain, M. M. Water Soluble Nano-Scale Transient Material Germanium Oxide for Zero Toxic Waste Based Environmentally Benign Nano-Manufacturing. *Appl. Phys. Lett.* **2017**, *110*, 074103.
(54) Pfau, A.; Schierbaum, K. D. The Electronic Structure of Stoichiometric and Reduced CeO2 Surfaces: An XPS, UPS and HREELS Study. *Surf. Sci.* **1994**, *321*, 71−80.
(55) Sharma, S.; Kumar, P. XPS Analysis of and Its-Substituted Alloy. *Mater. Today: Proc.* **2021**, *46*, 10597−10599.
(56) Rathnayake, R. M. N. M.; Wijayasinghe, H. W. M. A. C.; Pitawala, H. M. T. G. A.; Yoshimura, M.; Huang, H.-H. Synthesis of Graphene Oxide and Reduced Graphene Oxide by Needle Platy Natural Vein Graphite. *Appl. Surf. Sci.* **2017**, *393*, 309−315.
(57) Varga, M.; Izak, T.; Vretenar, V.; Kozak, H.; Holovsky, J.; Artemenko, A.; Hulman, M.; Skakalova, V.; Lee, D. S.; Kromka, A. Diamond/Carbon Nanotube Composites: Raman, FTIR and XPS Spectroscopic Studies. *Carbon* **2017**, *111*, 54−61.
(58) Lee, S.-W.; Lee, B.-J.; Oda, T. XPS Investigation and Field Emission Property of the Ar Plasma Processed Carbon Nanotube Films. *Trans. Electr. Electron. Mater.* **2008**, *9*, 52−56.
(59) Soin, N.; Roy, S. S.; Karlsson, L.; McLaughlin, J. A. Sputter Deposition of Highly Dispersed Platinum Nanoparticles on Carbon Nanotube Arrays for Fuel Cell Electrode Material. *Diamond Relat. Mater.* **2010**, *19*, 595−598.
(60) Amor, S. B.; Jacquet, M.; Fioux, P.; Nardin, M. XPS Characterisation of Plasma Treated and Zinc Oxide Coated PET. *Appl. Surf. Sci.* **2009**, *255*, 5052−5061.
(61) Le, Q. T.; Pireaux, J. J.; Verbist, J. J. Surface Modification of PET Films with RF Plasma and Adhesion Ofin Situ Evaporated Al on PET. *Surf. Interface Anal.* **1994**, *22*, 224−229.
(62) Velamakanni, A.; Magnuson, C. W.; Ganesh, K. J.; Zhu, Y.; An, J.; Ferreira, P. J.; Ruoff, R. S. Site-Specific Deposition of Au Nanoparticles in CNT Films by Chemical Bonding. *ACS Nano* **2010**, *4*, 540−546.
(63) Thamaraiselvan, C.; Lerman, S.; Weinfeld-Cohen, K.; Dosoretz, C. G. Characterization of a Support-Free Carbon Nanotube-Microporous Membrane for Water and Wastewater Filtration. *Sep. Purif. Technol.* **2018**, *202*, 1−8.
(64) Han, S.-H.; Kim, B.-J.; Park, J.-S. Effects of the Corona Pretreatment of PET Substrates on the Properties of Flexible Transparent CNT Electrodes. *Thin Solid Films* **2014**, *572*, 73−78.
(65) Shen, T.; Liu, Y.; Zhu, Y.; Yang, D.-Q.; Sacher, E. Improved Adhesion of Ag NPs to the Polyethylene Terephthalate Surface via Atmospheric Plasma Treatment and Surface Functionalization. *Appl. Surf. Sci.* **2017**, *411*, 411−418.
(66) Fernandez-Perez, A.; Marban, G. Visible Light Spectroscopic Analysis of Methylene Blue in Water; What Comes after Dimer? *ACS Omega* **2020**, *5*, 29801−29815.
(67) Ali, N.; Said, A.; Ali, F.; Raziq, F.; Ali, Z.; Bilal, M.; Reinert, L.; Begum, T.; Iqbal, H. M. N. Photocatalytic Degradation of Congo Red Dye from Aqueous Environment Using Cobalt Ferrite Nanostructures: Development, Characterization, and Photocatalytic Performance. *Water, Air, Soil Pollut.* **2020**, *231*, 50.
(68) Tahir, M. B.; Ashraf, M.; Rafique, M.; Ijaz, M.; Firman, S.; Mubeen, I. Activated Carbon Doped WO3 for Photocatalytic Degradation of Rhodamine-B. *Appl. Nanosci.* **2020**, *10*, 869−877.
(69) Huang, H.-B.; Wang, Y.; Jiao, W.-B.; Cai, F.-Y.; Shen, M.; Zhou, S.-G.; Cao, H.-L.; Lü, J.; Cao, R. Lotus-Leaf-Derived Activated-Carbon-Supported Nano-CdS as Energy-Efficient Photocatalysts under Visible Irradiation. *ACS Sustainable Chem. Eng.* **2018**, *6*, 7871−7879.
(70) Niedermeier, C. A.; Ide, K.; Katase, T.; Hosono, H.; Kamiya, T. Shallow Valence Band of Rutile GeO $_2$ and P-Type Doping. *J. Phys. Chem. C* **2020**, *124*, 25721−25728.
(71) Ahmad, A.; Jini, D.; Aravind, M.; Parvathiraja, C.; Ali, R.; Kiyani, M. Z.; Alothman, A. A Novel Study on Synthesis of Egg Shell Based Activated Carbon for Degradation of Methylene Blue via Photocatalysis. *Arabian J. Chem.* **2020**, *13*, 8717−8722.
(72) Hoc Thang, N.; Sy Khang, D.; Duy Hai, T.; Thi Nga, D.; Dinh Tuan, P. Methylene Blue Adsorption Mechanism of Activated Carbon Synthesised from Cashew Nut Shells. *RSC Adv.* **2021**, *11*, 26563−26570.
(73) Murugesan, A.; Loganathan, M.; Senthil Kumar, P.; Vo, D. V. N. Cobalt and Nickel Oxides Supported Activated Carbon as an Effective Photocatalysts for the Degradation Methylene Blue Dye from Aquatic Environment. *Sustainable Chem. Pharm.* **2021**, *21*, 100406.
(74) Le, H. A.; Linh, L. T.; Chin, S.; Jurng, J. Photocatalytic Degradation of Methylene Blue by a Combination of TiO 2-Anatase and Coconut Shell Activated Carbon. *Powder Technol.* **2012**, *225*, 167−175.
(75) Baruah, M.; Ezung, S. L.; Supong, A.; Bhomick, P. C.; Kumar, S.; Sinha, D. Synthesis, Characterization of Novel Fe-Doped TiO2 Activated Carbon Nanocomposite towards Photocatalytic Degradation of Congo Red, E. Coli, and S. Aureus. *Korean J. Chem. Eng.* **2021**, *38*, 1277−1290.
(76) Sun, J.-h.; Wang, Y.-k.; Sun, R.-x.; Dong, S.-y. Photodegradation of Azo Dye Congo Red from Aqueous Solution by the WO3-TiO2/Activated Carbon (AC) Photocatalyst under the UV Irradiation. *Mater. Chem. Phys.* **2009**, *115*, 303−308.
(77) Bendjabeur, S.; Zouaghi, R.; Kaabeche, O. N. H.; Sehili, T. Parameters Affecting Adsorption and Photocatalytic Degradation Behavior of Gentian Violet under UV Irradiation with Several Kinds

https://doi.org/10.1021/acsomega.3c03526
ACS Omega 2023, 8, 27663−27673

of TiO2as a Photocatalyst. *Int. J. Chem. React. Eng.* **2017**, *1*520160206. DOI: DOI: 10.1515/ijcre-2016-0206.
(78) Ma, M.; Ying, H.; Cao, F.; Wang, Q.; Ai, N. Adsorption of Congo Red on Mesoporous Activated Carbon Prepared by CO2 Physical Activation. *Chin. J. Chem. Eng.* **2020**, *28*, 1069−1076.
(79) Behnajady, M. A.; Modirshahla, N.; Hamzavi, R. Kinetic Study on Photocatalytic Degradation of C.I. Acid Yellow 23 by ZnO Photocatalyst. *J. Hazard. Mater.* **2006**, *133*, 226−232.
(80) Liu, Y.; Shen, L. From Langmuir Kinetics to First- and Second-Order Rate Equations for Adsorption. *Langmuir* **2008**, *24*, 11625−11630.
(81) Revellame, E. D.; Fortela, D. L.; Sharp, W.; Hernandez, R.; Zappi, M. E. Adsorption Kinetic Modeling Using Pseudo-First Order and Pseudo-Second Order Rate Laws: A Review. *Cleaner Engineering and Technology* **2020**, *1*, 100032.
(82) Tenri Ola, A. T.; Rahmat, R.; Fahri, A. N.; Heryanto, H.; Mutmainna, I.; Sesa, E.; Tahir, D. Synergistic Effect of Chitosan and Activated Carbon (AC) in Suppressing Recombination Charge of Composite $Ca_2Fe_2O_5$−AC/Chitosan for High Photodegradation of Fipronil Wastewater. *J. Polym. Environ.* **2022**, *30*, 3218−3229.
(83) Azizian, S. Kinetic Models of Sorption: A Theoretical Analysis. *J. Colloid Interface Sci.* **2004**, *276*, 47−52.
(84) Bullen, J. C.; Saleesongsom, S.; Gallagher, K.; Weiss, D. J. A Revised Pseudo-Second-Order Kinetic Model for Adsorption, Sensitive to Changes in Adsorbate and Adsorbent Concentrations. *Langmuir* **2021**, *37*, 3189−3201.
(85) Simonin, J.-P. On the Comparison of Pseudo-First Order and Pseudo-Second Order Rate Laws in the Modeling of Adsorption Kinetics. *J. Chem. Eng.* **2016**, *300*, 254−263.
(86) Lin, J.; Wang, L. Comparison between Linear and Non-Linear Forms of Pseudo-First-Order and Pseudo-Second-Order Adsorption Kinetic Models for the Removal of Methylene Blue by Activated Carbon. *Front. Environ. Sci. Eng. China* **2009**, *3*, 320−324.
(87) Natarajan, S.; Bajaj, H. C.; Tayade, R. J. Recent Advances Based on the Synergetic Effect of Adsorption for Removal of Dyes from Waste Water Using Photocatalytic Process. *Journal of Environmental Sciences* **2018**, *65*, 201−222.

https://doi.org/10.1021/acsomega.3c03526
ACS Omega 2023, 8, 27663−27673